SCIENCE CHINA
Technological Sciences

Special Topic: Coexisting-Cooperative-Cognitive (Tri-Co) Robot
•Article•

January 2019 Vol.62 No.1: 47–59
https://doi.org/10.1007/s11431-018-9348-9

A robotic laparoscopic tool with enhanced capabilities and modular actuation

DAI ZhengChen[1], WU ZhongHao[1], ZHAO JiangRan[1] & XU Kai[2*]

[1] *The RII Lab (Lab of Robotics Innovation and Intervention), UM-SJTU Joint Institute, Shanghai Jiao Tong University, Shanghai 200240, China;*
[2] *State Key Laboratory of Mechanical System and Vibration, School of Mechanical Engineering, Shanghai Jiao Tong University, Shanghai 200240, China*

Received June 14, 2018; accepted August 16, 2018; published online December 12, 2018

Due to the improved treatment outcomes, research on robotic MIS (Minimally Invasive Surgery) thrived in the past decades. A benchmark example is the da Vinci system that dominates robotic laparoscopy via its technology excellence and strong holding of intellectual properties. This study provides an alternative approach to realize robotic laparoscopic surgeries, by presenting the development and experimentation of the SMARLT (Strengthened Modularly Actuated Robotic Laparoscopic Tool) for MIS. A dual continuum mechanism is used in the design to achieve enhanced distal dexterity, improved reliability, increased payload capability, and actuation modularity. With kinematics modelling and actuation compensation, the SMARLT can be manipulated by a generic manipulator to carry out typical laparoscopic MIS tasks, such as tissue peeling, suturing, and knot tying. Payload capability was also experimentally characterized. The SMARLT-manipulator system essentially formed a continuum-rigid hybrid structure that makes full use of the advantages from each component: the continuum mechanism as a wrist for distal dexterity and other rigid parts for position accuracy and payload capability. With the experimental demonstration of the desired functionalities, the SMARLT design can lead to promising opportunities for commercialization.

dexterous wrist, dual continuum mechanism, medical robotics, modular laparoscopic tools, surgical instruments

Citation: Dai Z C, Wu Z H, Zhao J R, et al. A robotic laparoscopic tool with enhanced capabilities and modular actuation. Sci China Tech Sci, 2019, 62: 47–59, https://doi.org/10.1007/s11431-018-9348-9

1 Introduction

MIS (Minimally Invasive Surgery) has become a primary treatment option for numerous pathological conditions, due to its benefits of reduced postoperative complication rates, lower pain, and faster recovery [1].

Although laparoscopic MIS is beneficial, manual manipulations of the stick-like surgical tools can be exhausting and difficult, due to the inverted tool-manipulation movements and the lack of distal dexterity. Many surgical robotic systems were hence developed to assist surgeons in multi-port MIS for enhanced dexterity, augmented tactile sensing, better motion precision, more comfortable ergonomics, etc. [2].

Among the existing systems for robotic laparoscopic surgeries, the da Vinci robot has enabled many MIS procedures [3]. Even surgical paradigms with less invasiveness have emerged, such as SPL (Single Port Laparoscopy) [4] and NOTES (Natural Orifice Transluminal Endoscopic Surgery) [5]. Due to the limited accessibility to surgical sites and the challenges in system instrumentation, robotic assistance provided by the existing SPL/NOTES systems [6,7] has not fully enabled these less-invasive surgical procedures. Hence, considerable efforts still focus on laparoscopic surgical robotic systems.

*Corresponding author (email: k.xu@sjtu.edu.cn)

Aiming at outperforming the da Vinci robot, the existing research activities primarily have focused on enhancing: 1) the distal dexterity [8–15], 2) the force sensing capability [16–21], and 3) the design compactness and system modularity [13,22–24]. In order to propose an alternative design approach, the SMARLT was designed and constructed to realize robotic multi-port MIS, as shown in Figure 1. The SMARLT mainly consists of 1) an exchangeable effector with a continuum wrist, and 2) an actuation unit.

Other than providing the distal dexterity using the continuum wrist of the exchangeable effector, several performance enhancements of the SMARLT are considered during this development: 1) improved safety and reliability through redundant arrangement of the structural members, 2) increased payload capability, 3) applicable sterilization, and 4) actuation modularity. These capability enhancements are primarily gauged with respect to the existing surgical robots using continuum segments [25–27].

The SMARLT uses two motors to actuate the bending of the continuum wrist and a third motor to actuate the gripper. It can be fixed to and maneuvered by a generic manipulator (e.g., the Denso manipulator in Figure 1). The Denso manipulator can then deploy the SMARLT through a trocar to perform surgical tasks, serving as a programmable RCM (Remote Center of Motion) mechanism. The Denso manipulator orients and positions the SMARLT with respect to the trocar in order to minimize tearing to a patient's abdominal wall. A review of the RCM mechanisms is provided in ref. [28], while two new designs are presented in refs. [29,30].

The study's major contributions focus on: 1) the proposal of the SMARLT using the concept of dual continuum mechanism, and 2) the analytical kinematics framework for using the SMARLT (or similar ones) with a generic manipulator. The use of the newly proposed dual continuum mechanism from ref. [6] introduced several enhanced capabilities and actuation modularity, while the derived kinematics framework enabled the teleoperation of the SMARLT-manipulator system under the motion constraints resulting from the immobile skin incision port. Existing results on the constrained-movement kinematics [31–33] can't be directly used, since they don't explicitly include analytical formulations of the motions of the distal wrists. Minor contributions include: 1) the compact design of an actuation assembly for driving the exchangeable effector, and 2) the experimental characterizations of the SMARLT for the effectiveness demonstration.

A preliminary version of this paper was presented at the International Conference on Intelligent Robotics and Applications [34], which only introduced the design concept. The complete derivations of the constrained motion kinematics and the experimental characterizations of the SMARLT-Denso system are newly reported by this paper.

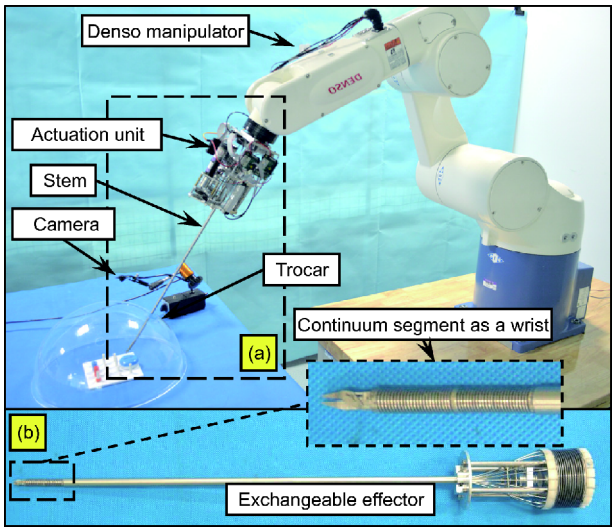

Figure 1 (Color online) The SMARLT attached to a manipulator. (a) The SMARLT; (b) the exchangeable effector.

2 Design objectives and overview

Aiming at facilitating robotic multi-port laparoscopic surgeries, the SMARLT is designed with its attachment to a generic manipulator, so that the tool-manipulator system (as in Figure 1) can be controlled for typical surgical tasks via teleoperation.

The design objectives are summarized as follows.

(1) The tool should include a 2-DoF (Degrees of Freedom) distal wrist for distal dexterity.

(2) The tool should support a modular actuation scheme, such that the surgical end effector can be replaced during a procedure for different tasks and the exchangeable part can be sterilized.

(3) The tool can be deployed through a trocar that is clinically used. This means that the tool's diameter should be less than 8 mm.

(4) When a hand tie is formed, the suture tension is usually less than 3 N [35,36]. When tissues are manipulated, the required force is usually from 1.3 N to 3.5 N [37]. According to the aforementioned investigations, the tool's payload capability is hence set at 3 N.

Attempting to satisfy the objectives above, the SMARLT is designed as in Figure 1(a), consisting of two major components.

The first component is an exchangeable effector. It has a straight stem with a length of 400 mm and an outer diameter of 7 mm. A continuum segment is installed at the stem's distal tip. The segment can bend to an arbitrary direction, providing a 2-DoF bending. Ideally, the bending radius of the segment should be as small as possible, such that the surgical end effector can be dexterously oriented at a confined surgical site. As explained in Section 3.1, the use of the dual continuum mechanism allows the use of many thin back-

bones in the distal wrist. Thinner backbones will help achieve smaller bending radii of the continuum wrist.

Different distal surgical end effectors can be attached to the distal end of the segment (currently a gripper is assembled). The exchangeable effector is entirely mechanical and enables convenient sterilization.

The second component is an actuation unit consisting of three actuation assemblies that drive the distal continuum wrist and the surgical end effector (currently a gripper).

3 System descriptions

A Denso manipulator was used to deploy and maneuver the SMARLT for typical surgical tasks in laparoscopic procedures. The exchangeable effector and the actuation unit are described in Section 3.1 and Section 3.2 respectively. The SMARLT's controller infrastructure is presented in Section 3.3.

3.1 Exchangeable effector with a continuum wrist

The exchangeable effector as in Figure 1(b) is shown in Figure 2. It used the dual continuum mechanism concept that was first proposed in ref. [6], where two stacked ones form a flexible manipulator. The mechanism's use here expands its applicability to form a continuum-rigid hybrid structure.

The exchangeable effector includes the following five components: 1) a gripper, 2) a distal continuum segment, 3) a straight stem, 4) several guiding channels, and 5) a proximal continuum segment. The distal and the proximal segments are structurally similar to the one in Figure 5(b). They are bent by pulling and pushing their backbones that are made from super-elastic nitinol rods.

As shown in Figure 2, the backbones of the exchangeable effector are passed through the distal segment, the straight stem, the guiding channels, and the proximal segment. The backbone arrangement in the distal segment is proportional to that in the proximal segment, forming a dual continuum mechanism. In this way, bending the proximal segment always bends the distal one in the opposite direction.

This dual continuum mechanism concept is different from the reciprocal mechanism in the RealHand instruments (Novare Surgical Systems, Inc.), where four cables are used for motion transmission. Since the cables should always be kept in tension, it is very difficult to integrate more cables. In the dual continuum mechanism, an arbitrary number of backbones can be arranged. Bending of the distal segment is collaboratively realized by all of the backbones.

Bending of the distal segment as a continuum wrist enhances the dexterity of the SMARLT during a laparoscopic procedure.

Strength of the distal continuum segment is affected by the

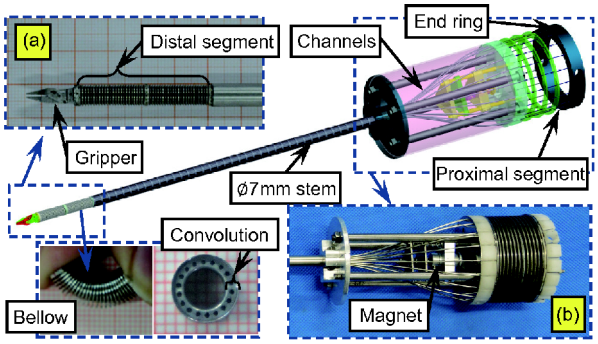

Figure 2 (Color online) The exchangeable effector of the SMARLT. (a) The distal segment as a wrist; (b) the proximal segment with the gripper actuation.

diameter and the number of the backbones. In order to achieve a higher payload, either thicker or more backbones shall be used. The use of thicker backbones would increase the backbones' minimal bending radius, if the same elastic strain is allowed. The tool's dexterity can then be affected, if a tight bending radius can't be achieved. Hence, more and thinner backbones should be used for a segment with a small bending radius and a high structural strength. The experimental study in ref. [38] is consistent with this design choice.

As indicated by the kinematics in Section 4.2, the distal segment possessed a 2-DoF bending. The use of the proximal segment for driving the distal segment then become truly necessary, since it is not efficient to use multiple servomotors to push or pull all of the backbones in the distal segment. The proximal segment always bends the distal one in the opposite direction, no matter how many backbones are arranged. It is explained in Section 3.2 how two actuators are used to drive the distal segment.

It is not enough to only increase the number of backbones. The experiments of weight lifting presented in ref. [39] indicate that the payload capability of a continuum segment significantly depends on its torsional stability. In order to increase the torsional stability without compromising the bending capability, two bellows (as in Figure 2) are used in the segment. The bellows' convolutions prevent the backbones from buckling under compressive loads.

The bellows are FC-4 series from Servometer LLC with an outer diameter of 6.35 mm and a free length of 18.8 mm. The stem's diameter of the SMARLT is set to 7 mm, so that the bellow can be connected to the stem. With the bellow customized, it is easy to design the exchangeable effectors with other diameters.

Eighteen ∅0.5-mm through holes were drilled in the bellows' convolutions by wire EDM to pass the backbones, as shown in Figure 2. The number of holes is determined by the manufacturing feasibility and the useable area in the bellows' convolutions.

Without compromising the bending capabilities for distal dexterity, the use of eighteen ∅0.4-mm backbones not only

increases the tool's payload capabilities, but also improves the tool's reliability. Even if one backbone is broken, the tool can still function as normal until the next inspection by the end of a procedure. For such a distal segment with eighteen ∅0.4-mm backbones, the minimal bending radius can reach 12.5 mm when the allowed elastic strain is 2%.

The dual continuum mechanism directly leads to beneficial actuation modularity. The distal segment and the straight stem can be set to different lengths and diameters, even with different surgical end effectors (e.g., scissors, grippers, and cautery spatula). When the same proximal segment is installed, the exchangeable effector can always be assembled into the actuation unit for the actuation of the distal segment. The only required update is to change the corresponding control parameters for the specific stem lengths and/or distal segment properties.

Actuation of the gripper is considered in the exchangeable effector design, as in Figure 2(b). The gripper's actuation rod is passed through a channel and connected to a spring-loaded reciprocating magnet. The magnet, which is used for quick connection with the actuation unit, is pushed and pulled to close and open the gripper, respectively. The spring avoids exerting excessive gripping forces.

The whole exchangeable effector only consists of mechanical parts. It can be sterilized by being emerged in glutaraldehyde or ortho-phthalaldehyde. However, since the exchangeable effector is still in a proof-of-concept stage, the sterilization is not clinically validated.

3.2 Actuation unit

The SMARLT's actuation unit is composed of 1) one driving segment, 2) two backbone driving assemblies, and 3) a gripper driving assembly, as presented in Figure 3.

The driving segment is structurally similar to the continuum segment in Figure 5(b). It is composed of a base ring, a few spacer rings, an end ring, and four backbones (∅1-mm nitinol rods). The inner diameter of the end ring of the driving segment in Figure 3 matches the outer diameter of the proximal segment of the exchangeable effector in Figure 2.

The actuation is realized by four driving backbones with only a pair of the driving backbones shown in Figure 5 for better visualization. When the proximal segment is manually assembled inside the driving segment, pushing-and-pulling actuation of the driving backbones bends the driving segment together with the proximal segment, so as to realize the bending of the distal segment.

Referring to the actuation kinematics in Section 4.2, the two driving backbones that are 180° apart should be pushed and pulled for the same distance simultaneously.

As shown in Figure 3(b), the two driving backbones are attached to a slider that is guided by a rail with a rack attached. A pinion, driven by a servomotor, drives the rack to push and pull the two driving backbones.

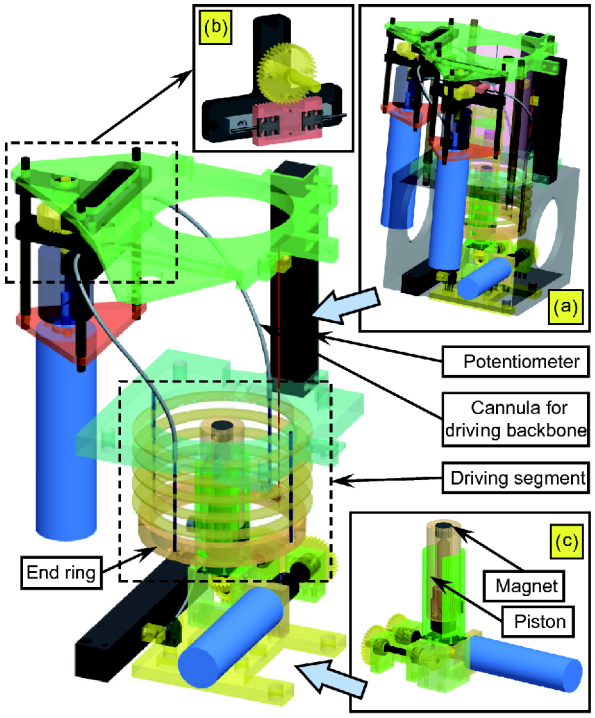

Figure 3 (Color online) The SMARLT's actuation unit. (a) The entire assembly; (b) the backbone driving assembly; (c) the gripper driving assembly.

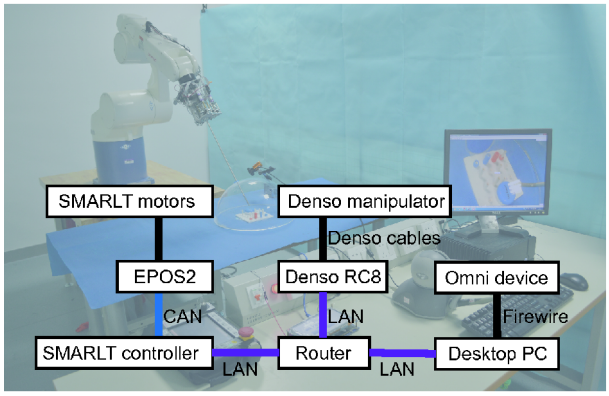

Figure 4 (Color online) The SMARLT's control infrastructure with the Denso manipulator.

In the gripper driving assembly, a lead screw is rotated by the third servomotor via a gear train, including two meshing spur gears and two meshing bevel gears. The nut of the lead screw is attached with a piston. On the top of the piston, a magnet is installed and allows quick connection to the other reciprocating magnet in the exchangeable effector. The attraction force between the two magnets is large enough for opening the gripper, while the piston pushes one magnet against the other to close the gripper.

Three linear potentiometers are arranged in the backbone

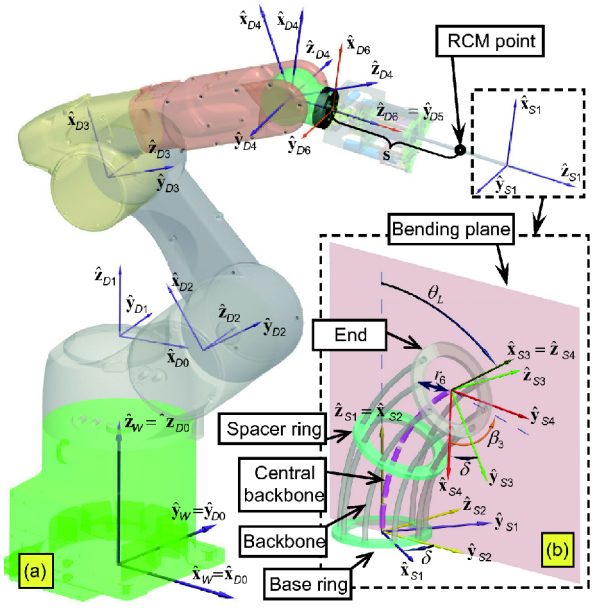

Figure 5 (Color online) Nomenclature and coordinates of the SMARLT-Denso system. (a) The Denso manipulator; (b) the bending segment.

driving assemblies and the gripper driving assembly, respectively, to sense the absolute positions of the driving backbones and the lead screw.

3.3 Control infrastructure

The control infrastructure of the SMARLT is constructed to allow teleoperation, controlling the SMARLT as well as a Denso manipulator that manipulates the SMARTL during a surgical procedure.

An Omni device is connected to a desktop computer via the IEEE 1394 firewire. The movement commands during teleoperation are continuously sent out via the desktop's LAN port following an UDP protocol.

The SMARLT's controller is an embedded system equipped with a 7-inch capacitive touch screen, a 1 GHz Cortex-A8 CPU, a CAN transceiver and a LAN port.

The controller runs a servo loop every 4 ms. During each servo loop, poses (including positions and orientations) of the Omni device are received and mapped as the desired poses for the SMARLT's gripper. The reference signals for the SMARLT and the manipulator are generated according to the inverse kinematics and the position and orientation inputs from the Omni device.

The reference signals are sent to the Denso RC8 controller in its slave mode via the LAN port using the UDP protocol to control the Denso manipulator. At the same time, the reference signals are sent to the three Maxon EPOS2 24/2 controllers via the CAN bus to control the SMARLT.

The three potentiometers in the actuation unit are read by the analog input ports of the EPOS2 digital controllers. The control infrastructure diagram is shown in Figure 4.

Each backbone driving assembly uses one Maxon 6-watt A-max-22 motor with a GP 22 A gearhead (gear ratio of 370:1) and a MR encoder (512 counts per turn). The gripper driving assembly uses one Maxon 2-watt A-max-16 motor with a GP 16 A gearhead (gear ratio of 29:1) and a MEnc 13 encoder (16 counts per turn). The total power rating of the system is approximately 3.5 kW with the majority of the power rating being the Denso manipulator.

4 Kinematics framework

The 2-DoF continuum segment is integrated in the SMARLT as a distal wrist, as shown in Figure 1. Kinematics of such a bending segment can refer to the studies in refs. [17,40,41]. For completeness, the kinematics of one bending segment is briefly summarized in Section 4.2 with the nomenclature defined in Section 4.1.

The Denso manipulator maneuvers the SMARLT through a skin incision. It essentially acts as a programmable RCM mechanism that positions and orients the SMARLT with respect to the incision point. Its use allows a flexible setting of the incision point in the abdominal wall.

The focus of the presented kinematics in Section 4.3 and Section 4.4 lies on the framework to use the SMARLT-Denso system as a continuum-rigid hybrid structure under the motion constraints stemmed from the immobile incision point in a patient's abdominal wall.

4.1 Nomenclature and coordinates

All of the segments in the SMARLT are structurally similar to the one shown in Figure 5(b). The segment's bent shapes can be approximated as circular arcs, referring to the analytical and experimental studies [17,40]. This assumption leads to the summarized kinematics in Section 4.2.

The following coordinates are defined with the nomenclature listed in Table 1 to describe the kinematics of the SMARLT and the Denso manipulator. The nomenclature is adopted from the preliminary version of this study [34].

World Coordinate $\{W\} \equiv \{\hat{\mathbf{x}}_W, \hat{\mathbf{y}}_W, \hat{\mathbf{z}}_W\}$ (or $\{D0\} \equiv \{\hat{\mathbf{x}}_{D0}, \hat{\mathbf{y}}_{D0}, \hat{\mathbf{z}}_{D0}\}$) is located at the base of the Denso manipulator.

Denso Coordinates $\{Dj\} \equiv \{\hat{\mathbf{x}}_{Dj}, \hat{\mathbf{y}}_{Dj}, \hat{\mathbf{z}}_{Dj}\}$ $(j = 1, 2, \cdots, 6)$ are assigned to the joint axes of the Denso manipulator.

Segment Base Coordinate $\{S1\} \equiv \{\hat{\mathbf{x}}_{S1}, \hat{\mathbf{y}}_{S1}, \hat{\mathbf{z}}_{S1}\}$ is attached to the segment's base ring. The XY plane is aligned with the base ring with its origin at the center. $\{S1\}$ is translated from $\{D6\}$ by a distance h in the $\hat{\mathbf{z}}_{D6}$ direction. $\hat{\mathbf{x}}_{S1}$ points from the center to the 1st backbone.

Table 1 Nomenclature used in this study.

Symbol	Definition
j	Index of the Denso manipulator axes, j = 1, 2,⋯, 6
$_j$	Joint variables of the Denso manipulator
$\boldsymbol{\Psi}_D$	$\boldsymbol{\Psi}_D \equiv [\varphi_1\ \varphi_2\ \cdots\ \varphi_6]^{\mathrm{T}}$ is the manipulator's configuration vector.
s	Distance along the SMARLT's stem from the{$D6$}origin to the RCM point
h	Distance between the origins of {$D6$} and {$S1$}along the SMARLT's stem
i	Index of the segment backbones, i = 1, 2,⋯, m
r_i	Distance from the virtual central backbone to the ith backbone
$_i$	Division angle from the ith backbone to the 1st backbone; β_1=0 and β_i remain constant once the segment is built
	Size ratio between a distal segment and a proximal one
L, L_i	Lengths of the central backbone and the ith backbone measured from the base ring to the end ring along the backbones
q_i	Push-pull actuation of the segment's ith backbone; $q_i \equiv L_i - L$
$_i$	A right-handed rotation angle about $\hat{\mathbf{z}}_{S1}$ from $\hat{\mathbf{y}}_{S2}$ to a ray passing through the central backbone and the ith backbone. $\delta \equiv \delta_1$ and $\delta_i = \delta + \beta_i$
$_L$	The right-handed rotation angle from $\hat{\mathbf{x}}_{S2}$ to $\hat{\mathbf{x}}_{S3}$.
$\boldsymbol{\Psi}_S$	$\boldsymbol{\Psi}_S \equiv [\theta_L\ \delta]^{\mathrm{T}}$ is the segment's configuration vector.
$\boldsymbol{\Psi}$	$\boldsymbol{\Psi} \equiv [\boldsymbol{\Psi}_D{}^T\ \boldsymbol{\Psi}_S{}^T]^{\mathrm{T}}$ is the configuration vector of the entire system.
$^{S1}\mathbf{p}_L$	Center position of the segment's end ring in{$S1$}
$^1\mathbf{R}_2$	Coordinate transformation matrix from frame 2 to frame 1
$^1\mathbf{T}_2$	Homogeneous transformation matrix from frame 2 to frame 1

Segment Base Bending Coordinate $\{S2\} \equiv \{\hat{\mathbf{x}}_{S2}, \hat{\mathbf{y}}_{S2}, \hat{\mathbf{z}}_{S2}\}$ shares its origin with $\{S1\}$ and has the segment bending in its XY plane.

Segment Tip Bending Coordinate $\{S3\} \equiv \{\hat{\mathbf{x}}_{S3}, \hat{\mathbf{y}}_{S3}, \hat{\mathbf{z}}_{S3}\}$ is obtained from $\{S2\}$ by a rotation about $\hat{\mathbf{z}}_{S2}$, such that $\hat{\mathbf{x}}_{S3}$ becomes the backbone tangent at the end ring. Origin of $\{S3\}$ is at the center of the end ring.

Segment Tip Coordinate $\{S4\} \equiv \{\hat{\mathbf{x}}_{S4}, \hat{\mathbf{y}}_{S4}, \hat{\mathbf{z}}_{S4}\}$ is fixed to the end ring. $\hat{\mathbf{x}}_{S4}$ points from the end ring center to the first backbone and $\hat{\mathbf{z}}_{S4}$ is normal to the end ring.

4.2 Kinematics of the continuum segment

As shown in Figure 5(b), the backbones are pulled and pushed simultaneously to bend the segment. The length and shape of the segment is characterized by a central backbone. Even when the central backbone is absent, a virtual central backbone still indicates the length and shape [17,40].

The backbones are assumed to have circular shapes in planes parallel to the bending plane. The lengths of the central backbone and the ith backbone are related as obtained in eq. (1). The backbone actuation is then written in eq. (2), according to the definition of q_i.

$$L_i = L - r_i\theta_L\cos(\delta+\beta_i). \tag{1}$$

$$q_i = -r_i\theta_L\cos(\delta+\beta_i). \tag{2}$$

To drive the continuum segment to a configuration or pose specified by $\boldsymbol{\Psi}_s$, each backbone should be actuated, referring to the actuation kinematics in eq. (2).

It can be clearly seen from the actuation kinematics that the bending is a 2-DoF one, since all q_i depend on two variables (θ_L and δ). All of the backbones should be coordinately and simultaneously actuated. Obviously, it is not wise to use eighteen servomotors. Therefore, the proximal segment is necessary to realize the coordinate push-pull actuation for the eighteen backbones in the distal segment.

The backbone arrangements in the distal and the proximal segments should satisfy the conditions of $(r_i)_{\text{proximal}}=(\kappa r_i)_{\text{distal}}$ and $(\beta_i)_{\text{proximal}}=(\beta_i)_{\text{distal}}$. Therefore, a bending of θ_L and δ on the distal segment corresponds to a bending of θ_L/κ and $\delta+\pi$ on the proximal segment. Because the driving and the proximal segments always have the same shape, the four driving backbones shall be actuated, referring to eq. (3), with the bending configuration variables (θ_L/κ and $\delta+\pi$), using the structural parameters from Table 2.

$$\begin{cases} q_1 = -(r_i)_{\text{driving}}\dfrac{\theta_L}{\kappa}\cos(\delta+\pi) = -q_3, \\ q_2 = -(r_i)_{\text{driving}}\dfrac{\theta_L}{\kappa}\cos\left(\delta+\dfrac{3\pi}{2}\right) = -q_4, \end{cases}$$

$$\kappa = \frac{(r_i)_{\text{proximal}}}{(r_i)_{\text{distal}}}. \tag{3}$$

The distal segment has a circular shape and the center

Table 2 Structural parameters of the SMARLT-Denso system.

Denavit-Hartenberg parameters of the Denso manipulator					Distal segment	
					r_i = 2.5 mm	L = 40 mm
No.	α_{j-1}	a_{j-1}	d_j	φ_j	Proximal segment	
1	0	0	473 mm	φ_1	r_i = 24 mm	L = 35 mm
2	–π/2	180 mm	0	φ_2–π/2	Driving segment	
3	0	385 mm	0	φ_3	r_i = 30 mm	L = 35 mm
4	–π/2	100 mm	445 mm	φ_4	β_i = 0, π/2, π, 3π/2	
5	π/2	0	0	φ_5	Translation	h = 580 mm
6	–π/2	0	90 mm	φ_6	Gripper tip	g = 15 mm

position of the end ring is as follows.

$$ {}^{S1}\mathbf{p}_L = \frac{L}{\theta_L}\left[\cos\delta(1-\cos\theta_L) \quad \sin\delta(\cos\theta_L-1) \quad \sin\theta_L\right]^{\mathrm{T}}, \tag{4} $$

where ${}^{S1}\mathbf{p}_L = [0 \quad 0 \quad L]^{\mathrm{T}}$ when $\theta_L \to 0$.

Transformation matrix ${}^{S1}\mathbf{R}_{S4}$ relates $\{S4\}$ to $\{S1\}$.

$$ {}^{S1}\mathbf{R}_{S4} = {}^{S1}\mathbf{R}_{S2}\,{}^{S2}\mathbf{R}_{S3}\,{}^{S3}\mathbf{R}_{S4}, \tag{5} $$

where

$$ {}^{S1}\mathbf{R}_{S2} = \begin{bmatrix} 0 & \cos\delta & \sin\delta \\ 0 & -\sin\delta & \cos\delta \\ 1 & 0 & 0 \end{bmatrix}, $$

$$ {}^{S2}\mathbf{R}_{S3} = \begin{bmatrix} \cos\theta_L & -\sin\theta_L & 0 \\ \sin\theta_L & \cos\theta_L & 0 \\ 0 & 0 & 1 \end{bmatrix}, $$

and

$$ {}^{S3}\mathbf{R}_{S4} = \begin{bmatrix} 0 & 0 & 1 \\ \cos\delta & -\sin\delta & 0 \\ \sin\delta & \cos\delta & 0 \end{bmatrix}. $$

The segment's instantaneous kinematics from the segment configuration space to the task space, with respect to the end ring center, is as follows.

$$ {}^{S1}\dot{\mathbf{x}} = \mathbf{J}_S\dot{\boldsymbol{\psi}}_S = \begin{bmatrix} \mathbf{J}_{vS} \\ \mathbf{J}_{\omega S} \end{bmatrix}\dot{\boldsymbol{\psi}}_S, \tag{6} $$

where ${}^{S1}\mathbf{v} = \mathbf{J}_{vS}\dot{\boldsymbol{\psi}}_S$ and ${}^{S1}\boldsymbol{\omega} = \mathbf{J}_{\omega S}\dot{\boldsymbol{\psi}}_S$.

$$ \mathbf{J}_{vS} = L\begin{bmatrix} \cos\delta\left(\dfrac{\cos\theta_L-1}{\theta_L^2}+\dfrac{\sin\theta_L}{\theta_L}\right) & \dfrac{\sin\delta}{\theta_L}(\cos\theta_L-1) \\ \sin\delta\left(\dfrac{1-\cos\theta_L}{\theta_L^2}-\dfrac{\sin\theta_L}{\theta_L}\right) & \dfrac{\cos\delta}{\theta_L}(\cos\theta_L-1) \\ -\dfrac{\sin\theta_L}{\theta_L^2}+\dfrac{\cos\theta_L}{\theta_L} & 0 \end{bmatrix}, \tag{7} $$

$$ \mathbf{J}_{\omega S} = \begin{bmatrix} \sin\delta & \cos\delta\sin\theta_L \\ \cos\delta & -\sin\delta\sin\theta_L \\ 0 & \cos\theta_L-1 \end{bmatrix}. \tag{8} $$

4.3 Kinematics of the denso manipulator

The Denavit-Hartenberg parameters [42] listed in Table 2 can be conveniently used to describe the kinematics of the Denso manipulator. The homogeneous transformation matrix is as follows.

$$ {}^{D(j-1)}\mathbf{T}_{Dj} = \begin{bmatrix} {}^{D(j-1)}\mathbf{R}_{Dj} & {}^{D(j-1)}\mathbf{p} \\ \mathbf{0}_{1\times3} & 1 \end{bmatrix}, \tag{9} $$

where j = 1, 2, ⋯, 6,

$$ {}^{D(j-1)}\mathbf{R}_{Dj} = \begin{bmatrix} \cos\varphi_j & -\sin\varphi_j & 0 \\ \sin\varphi_j\cos\alpha_{i-1} & \cos\varphi_j\cos\alpha_{i-1} & -\sin\alpha_{i-1} \\ \sin\varphi_j\sin\alpha_{i-1} & \cos\varphi_j\sin\alpha_{i-1} & \cos\alpha_{i-1} \end{bmatrix}, $$

and

$$ {}^{D(j-1)}\mathbf{p} = \left[a_{j-1} \quad -d_j\sin\alpha_{i-1} \quad d_j\cos\alpha_{i-1}\right]^{\mathrm{T}}. $$

The Jacobian matrix $\mathbf{J}_D$ of the Denso manipulator with respect to the center of its distal flange can be easily derived in eqs. (10)–(12). The SMARLT is attached to the Denso manipulator at this flange.

$$ {}^{D0}\dot{\mathbf{x}} = \mathbf{J}_D\dot{\boldsymbol{\psi}}_D = \begin{bmatrix} \mathbf{J}_{vD} \\ \mathbf{J}_{\omega D} \end{bmatrix}\dot{\boldsymbol{\psi}}_D, \tag{10} $$

where ${}^{D0}\mathbf{v} = \mathbf{J}_{vD}\dot{\boldsymbol{\psi}}_D$ and ${}^{D0}\boldsymbol{\omega} = \mathbf{J}_{\omega D}\dot{\boldsymbol{\psi}}_D$, $\mathbf{J}_{vD}, \mathbf{J}_{\omega D} \in \Re^{3\times6}$.

$$ \begin{aligned} &\mathbf{J}_{vD} \\ &= \left[{}^{D0}\hat{\mathbf{z}}_{D1}\times{}^{D0}\mathbf{p}_{D1D6} \quad {}^{D0}\hat{\mathbf{z}}_{D2}\times{}^{D0}\mathbf{p}_{D2D6} \quad {}^{D0}\hat{\mathbf{z}}_{D3}\times{}^{D0}\mathbf{p}_{D3D6}\right. \\ &\quad \left.\dot{\varphi}_4\,{}^{D0}\hat{\mathbf{z}}_{D4}\times{}^{D0}\mathbf{p}_{D4D6} \quad \dot{\varphi}_5\,{}^{D0}\hat{\mathbf{z}}_{D5}\times{}^{D0}\mathbf{p}_{D5D6} \quad \mathbf{0}\right]. \end{aligned} \tag{11} $$

$$\mathbf{J}_{\omega D}=\begin{bmatrix}{}^{D0}\hat{\mathbf{z}}_{D1} & {}^{D0}\hat{\mathbf{z}}_{D2} & {}^{D0}\hat{\mathbf{z}}_{D3} & {}^{D0}\hat{\mathbf{z}}_{D4} & {}^{D0}\hat{\mathbf{z}}_{D5} & {}^{D0}\hat{\mathbf{z}}_{D6}\end{bmatrix}. \quad (12)$$

The 6th column of $\mathbf{J}_{vD}$ is entirely zero, because the rotation of the 6th joint does not introduce any linear velocity at the center of the distal flange.

4.4 Kinematics with constrained motions and teleoperation

The SMARLT is attached to the distal flange of the Denso manipulator, with $\{S1\}$ translated from $\{D6\}$ by a constant distance of h along the tool stem: ${}^{D6}\mathbf{p}_{\text{Seg}}=[0\ 0\ h]^{\text{T}}$. A gripper (or another surgical end effector) is installed to the end ring of the SMARLT's segment. The tip position of the gripper is located at ${}^{S4}\mathbf{p}_{gp}=[0\ 0\ g]^{\text{T}}$ in $\{S4\}$. The h and g values are listed in Table 2, whereas the h value accounts for the lengths of the stem and the actuation unit. The grippzer tip position in $\{D0\}$ can then be obtained as in eq. (13).

$$\begin{bmatrix}{}^{D0}\mathbf{p}_{gp} & 1\end{bmatrix}^{\text{T}}={}^{D0}\mathbf{T}\begin{bmatrix}{}^{S4}\mathbf{p}_{gp} & 1\end{bmatrix}^{\text{T}}, \quad (13)$$

where ${}^{D0}\mathbf{T}=\prod_{j=1}^{6}{}^{D(j-1)}\mathbf{T}_{Dj}\cdot\begin{bmatrix}\mathbf{I}_{3\times3} & {}^{D6}\mathbf{p}_{\text{Seg}}\\ \mathbf{0}_{1\times3} & 1\end{bmatrix}\begin{bmatrix}{}^{S1}\mathbf{R}_{S4} & {}^{S1}\mathbf{p}_{L}\\ \mathbf{0}_{1\times3} & 1\end{bmatrix}$ and ${}^{S1}\mathbf{p}_{L}$ is from eq. (4).

The SMARLT is deployed and maneuvered by the Denso manipulator through a skin incision. The incision point (the RCM point in Figure 5) can translate with respect to the SMARTL's stem, while its lateral movements should be limited to minimize possible tear to a patient's abdominal wall.

The RCM point imposes a constraint to the movements of the SMARLT-Denso system. Although it is possible to design a virtual-fixture-based controller to maintain the constraints [43], this study chooses a kinematics approach similar to the ones presented in refs. [31–33] due to the limited access to the motion controller of the Denso manipulator.

This study generalizes the aforementioned studies [31–33] by directly using the manipulator Jacobian $\mathbf{J}_D$ and the tool Jacobian $\mathbf{J}_S$ to formulate a prioritized inverse kinematics. The presented approach only concerns the RCM point, while the aforementioned existing studies [31–33] involve two points on the tool stem or the stem's orientation.

The RCM point is located at ${}^{D6}\mathbf{p}_{\text{RCM}}=[0\ 0\ s]^{\text{T}}$ in $\{D6\}$. Its linear velocity can be formulated as in eq. (14). The component that is perpendicular to the stem can be derived as in eq. (15), with the matrix form in eq. (16).

$${}^{D0}\mathbf{v}_{\text{RCM}}=\mathbf{J}_{vD}\dot{\boldsymbol{\psi}}_D+\mathbf{J}_{\omega D}\dot{\boldsymbol{\psi}}_D\times{}^{D0}\mathbf{R}_{D6}{}^{D6}\mathbf{p}_{\text{RCM}}. \quad (14)$$

$${}^{D0}\mathbf{v}_{\text{RCM}\perp}={}^{D0}\mathbf{v}_{\text{RCM}}-\left({}^{D0}\mathbf{v}_{\text{RCM}}\cdot{}^{D0}\hat{\mathbf{z}}_{D6}\right){}^{D0}\hat{\mathbf{z}}_{D6}. \quad (15)$$

$$\begin{aligned}{}^{D0}\mathbf{v}_{\text{RCM}\perp}&=\mathbf{J}_{\text{RCM}\perp}\dot{\boldsymbol{\psi}}\\&=\left(\mathbf{I}-{}^{D0}\hat{\mathbf{z}}_{D6}{}^{D0}\hat{\mathbf{z}}_{D6}^{\text{T}}\right)\\&\quad\begin{bmatrix}\mathbf{J}_{vD} & -\left[{}^{D0}\mathbf{R}_{D6}{}^{D6}\mathbf{p}_{\text{RCM}}\times\right]\mathbf{J}_{\omega D} & \mathbf{0}\end{bmatrix}\dot{\boldsymbol{\psi}},\end{aligned} \quad (16)$$

where $[\mathbf{p}\times]$ is the skew-symmetric matrix of the vector $\mathbf{p}$.

The gripper (or another surgical end effector) is installed to the end ring of the SMARLT's segment. The tip position of the gripper is located at ${}^{S4}\mathbf{p}_{\text{gp}}=[0\ 0\ g]^{\text{T}}$ in $\{S4\}$. The twist of the SMARLT tip can then be formulated as in eq. (17).

$${}^{D0}\dot{\mathbf{x}}_{\text{Tip}}=\begin{bmatrix}{}^{D0}\mathbf{v}_{\text{Tip}}\\ {}^{D0}\boldsymbol{\omega}_{\text{Tip}}\end{bmatrix}=\mathbf{J}_{\text{Tip}}\dot{\boldsymbol{\psi}}=\begin{bmatrix}\mathbf{J}_{v\text{Tip}}\\ \mathbf{J}_{\omega\text{Tip}}\end{bmatrix}\dot{\boldsymbol{\psi}}, \quad (17)$$

$$\begin{aligned}{}^{D0}\mathbf{v}_{\text{Tip}}&=\mathbf{J}_{vD}\dot{\boldsymbol{\psi}}_D+\mathbf{J}_{\omega D}\dot{\boldsymbol{\psi}}_D\times{}^{D0}\mathbf{R}_{D6}{}^{D6}\mathbf{p}_{\text{Seg}}\\&\quad+{}^{D0}\mathbf{R}_{D6}\left(\mathbf{J}_{vS}\dot{\boldsymbol{\psi}}_S+\mathbf{J}_{\omega S}\dot{\boldsymbol{\psi}}_S\times{}^{S1}\mathbf{R}_{S4}{}^{S4}\mathbf{p}_{gp}\right)\\&=\left[\mathbf{J}_{vD}-\left[{}^{D0}\mathbf{R}_{D6}{}^{D6}\mathbf{p}_{\text{Seg}}\times\right]\mathbf{J}_{\omega D}\right.\\&\quad\left.{}^{D0}\mathbf{R}_{D6}\left(\mathbf{J}_{vS}-\left[{}^{S1}\mathbf{R}_{S4}{}^{S4}\mathbf{p}_{gp}\times\right]\mathbf{J}_{\omega S}\right)\right]\dot{\boldsymbol{\psi}},\end{aligned} \quad (18)$$

where ${}^{D6}\mathbf{p}_{\text{Seg}}=[0\ 0\ h]^{\text{T}}$ is the translation from $\{S1\}$ to $\{D6\}$.

$${}^{D0}\boldsymbol{\omega}_{\text{Tip}}=\mathbf{J}_{\omega D}\dot{\boldsymbol{\psi}}_D+{}^{D0}\mathbf{R}_{D6}\mathbf{J}_{\omega S}\dot{\boldsymbol{\psi}}_S=\begin{bmatrix}\mathbf{J}_{\omega D} & {}^{D0}\mathbf{R}_{D6}\mathbf{J}_{\omega S}\end{bmatrix}\dot{\boldsymbol{\psi}}. \quad (19)$$

While the SMARLT-Denso system is teleoperated for surgical tasks under the motion constraint imposed by the RCM point, the primary task is to maintain the constraint, and the secondary task is to reach a desired position (and orientation). The primary and the secondary tasks are indicated by eq. (16) and (17), respectively. As shown in ref. [44], the constrained inverse kinematics can be written in eq. (20), treating the primary task as a constraint. When the constraint is $\mathbf{v}_{\text{RCM}\perp}=\mathbf{0}$, eq. (20) gives eq. (21).

$$\begin{aligned}\dot{\boldsymbol{\psi}}&=\mathbf{J}_{\text{RCM}\perp}^{+}\mathbf{v}_{\text{RCM}\perp}\\&\quad+\left(\mathbf{I}-\mathbf{J}_{\text{RCM}\perp}^{+}\mathbf{J}_{\text{RCM}\perp}\right)\mathbf{J}_{\text{RT}}^{+}\left(\dot{\mathbf{x}}_{\text{Tip}}-\mathbf{J}_{\text{Tip}}\mathbf{J}_{\text{RCM}\perp}^{+}\mathbf{v}_{\text{RCM}\perp}\right).\end{aligned} \quad (20)$$

$$\dot{\boldsymbol{\psi}}=\left(\mathbf{I}-\mathbf{J}_{\text{RCM}\perp}^{+}\mathbf{J}_{\text{RCM}\perp}\right)\mathbf{J}_{\text{RT}}^{+}\dot{\mathbf{x}}_{\text{Tip}}, \quad (21)$$

where $\mathbf{J}^{+}$ is the pseudo-inverse of the Jacobian matrix $\mathbf{J}$ and $\mathbf{J}_{\text{RT}}=\mathbf{J}_{\text{Tip}}\left(\mathbf{I}-\mathbf{J}_{\text{RCM}\perp}^{+}\mathbf{J}_{\text{RCM}\perp}\right)$.

Using the prioritized inverse kinematics as in eq. (21), the SMARLT-Denso system can be teleoperated according to the scheme depicted in Figure 6. With the difference between the current and the desired position and orientation of the gripper, $\dot{\mathbf{x}}_{\text{Tip}}$ is first obtained. $\dot{\boldsymbol{\psi}}$ is then calculated using eq. (21). The translational velocity of the RCM point with respect to the stem can be obtained using eq. (16). The increments of the RCM position Δs and the system configuration $\Delta\boldsymbol{\Psi}$ can then be obtained. Using the updated s and $\boldsymbol{\Psi}$, the Denso manipulator is instructed and the segment is actuated according to the actuation kinematics in eq. (2) and (3). The

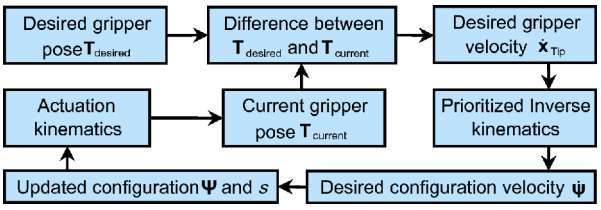

Figure 6 (Color online) Teleoperation of the SMARLT-Denso system.

gripper position is updated according to eq. (13).

The inverse kinematics involves the calculation of the pseudo-inverse of different Jacobian matrices. The singularity-robust formulation from ref. [42] is used as in eq. (22).

$$\mathbf{J}^{+}=\begin{cases}\mathbf{J}^{T}(\mathbf{J}\mathbf{J}^{T}+\lambda\mathbf{I})^{-1}, \sigma_{\min}<\varepsilon\\ \mathbf{J}^{T}(\mathbf{J}\mathbf{J}^{T})^{-1}, \text{otherwise},\end{cases} \tag{22}$$

where σ_{min} is the non-zero smallest singular value, λ and ε are small positive values (both 0.02 in this implementation).

5 Experimental characterizations

With the SMARLT constructed and the kinematics derived, a series of experiments were conducted to demonstrate the performances of this device.

5.1 Actuation Compensation

Previous studies in refs. [6,25,45] show that when the actuation lengths are commanded according to eq. (2) and (3), the segment of the SMARLT usually bends less than the desired angle, even though the bent shapes can still be approximated as circular arcs. Hence, actuation compensation should be formulated based on a bending calibration process.

The bending calibration is conducted as follows. From a straight shape, the continuum segment is driven to several desired bending angles specified by θ_L. The issued actuation lengths are obtained according to eq. (3). An optical tracker (Micron Tracker SX60, Claron Technology, Inc.) is used to identify the actual bending angles, as shown in Figure 7(a). The desired and actual bending angles are plotted in Figure 7 (b).

The θ_L value was first assigned from 0° to 130°. Due to the backlash in the actuation unit, the segment did not immediately bend back when θ_L was reduced and the segment did not return to the straight configuration when θ_L was reduced to 0°. Negative θ_L values were issued until the segment was completely straightened. Then, the θ_L value was increased again for more measurements.

Backlashes in the two backbone driving assemblies were obtained by reading the motor encoders while observing the segment movements. The backlashes for q_1 and q_2 are

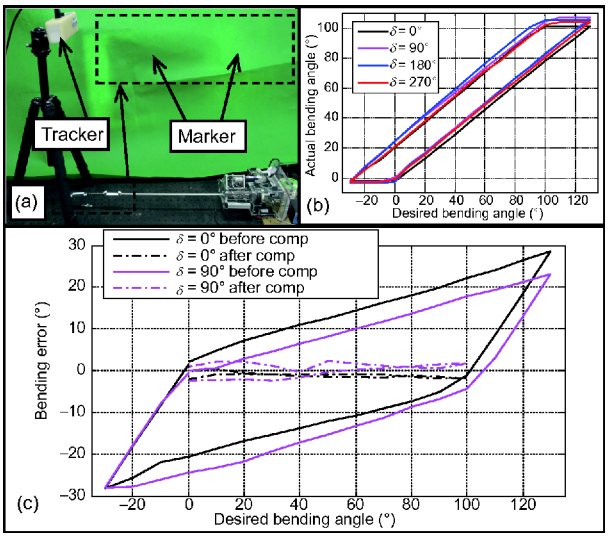

Figure 7 (Color online) Calibration of the SMARLT-Denso system. (a) Setup; (b) bending measurements; (c) bending errors before and after compensation.

1.472 mm and 1.636 mm, respectively. These are from the gearhead, the rack-pinion connection, the compliance of the coupling, and the structural elasticity of the backbone driving assemblies.

The backlashes were diminished by a proper initialization and directional compensation. The segment was first bent by setting q_1 and q_2 to negative values. Then, q_1 and q_2 were increased till the segment became straight. And the q_1 and q_2 values were reset and the actuation of the SMARLT started from this straight configuration. Every time q_1 or q_2 changed movement direction, an additional distance at the amount of the backlash would be actuated. This directional compensation for backlash will not drift, since the compensation is referenced back to the raw encoder values.

With the backlashes diminished, the actuation compensation was formulated as follows.

$$\begin{cases}q_1=-C_1(r_i)_{\text{driving segment}}(\theta_L/\kappa)\cos(\delta+\pi),\\ q_2=-C_2(r_i)_{\text{driving segment}}(\theta_L/\kappa)\cos(\delta+3\pi/2),\end{cases} \tag{23}$$

where C_1=1.24 and C_2=1.245. Both coefficients were obtained by linear regression of the measurement results.

With the compensation implemented on θ_L and backlashes diminished, the bending errors were significantly reduced, as shown in Figure 7(c). Due to the backbones' redundant arrangement, no compensation was conducted on δ.

5.2 Stiffness characterization

When the continuum segment of the SMARLT is subject to external loads, it would be further deformed from the assumed circular shape. When the external load is large enough (even though the structure doesn't fail), there might be severe

bending discrepancy between the actual and the assumed shapes such that teleoperation can be difficult even under real-time visual feedback. Hence, the stiffness of the continuum segment is characterized here to indicate how external loads affect the motion accuracy. Ultimate payload capability is shown by the weight-lifting experiments as in Section 5.4. Such a loading condition should only occur in the scenarios where motion accuracy is not crucial, such as tightening a knot.

The experimental setup is shown in Figure 8(a). A 3D force sensor (K3D60 with measurement ranges of ±50 N in the *XYZ* directions from ME-Meßsysteme GmbH) is attached to a Cartesian motion stage. A 3D printed probe is connected to the sensor. A DAQ card (Advantech PCL-818HG) was used to achieve a sensing accuracy of 0.04 N. The experimental setup was referred to the existing studies [12,38].

The continuum segment was set straight or bent to several desired θ_L angles. The probe was first positioned by the motion stage to touch the gripper tip. The motion stage then moved the probe to perturb the gripper for a few millimeters in the $\hat{\mathbf{x}}_{S1}$- and $\hat{\mathbf{y}}_{S1}$-directions. The probe is rigid enough such that the movements of the probe represent the deflection of the continuum segment. The reaction forces in the $\hat{\mathbf{x}}_{S1}$-direction were measured and plotted with respect to the deflections, as shown in Figure 8(b). A slope can be fitted to the measurements to estimate the stiffness (forces per millimeter). The stiffness of the continuum segment in the $\hat{\mathbf{x}}_{S1}$- and $\hat{\mathbf{y}}_{S1}$-directions with respect to different θ_L angles are plotted in Figure 8(c).

The measurement errors may include: 1) the sensing errors of the force senor with 0.2% linearity, 2) the A/D acquisition errors, and 3) possible probe-movement deviations from the desired $\hat{\mathbf{x}}_{S1}$- and $\hat{\mathbf{y}}_{S1}$-directions.

The results in Figure 8(c) show that the stiffness is approximately five to sixteen times higher than that of the continuum manipulator from the previous study [6], due to the reduced segment length. With the obtained stiffness, the SMARLT-Denso system can be teleoperated for surgical tasks. Even with positioning errors of a few millimeters under a 3 N load, a human operator can knowingly correct this discrepancy under visual feedback.

5.3 Constrained motions of the SMARLT-Denso system

The teleoperation of the SMARLT-Denso system is initiated, setting the distal wrist of the SMARLT to be straight. The Denso manipulator is then commanded to insert the wrist of the SMARLT through the trocar using the Denso's teaching panel. The insertion should continue until the $\{S1\}$ origin is at the trocar point (namely the segment's base ring is aligned with the trocar). Under this configuration, s=h. The teleoperation starts subsequently according to the kinematics

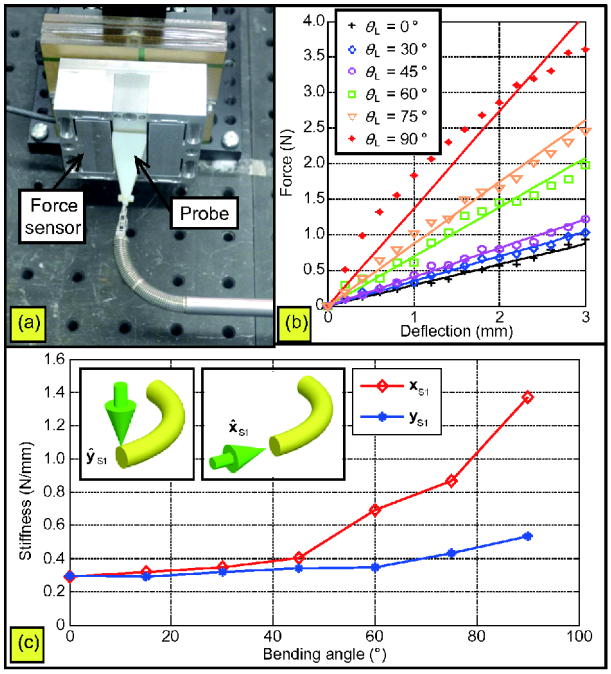

Figure 8 (Color online) Stiffness characterizations of the SMARLT. (a) Experimental setup; (b) force with respect to deflection under different poses; (c) obtained stiffness with the two insets showing the loading directions.

presented in Section 5.4.

The SMARLT-Denso system is planned to move across a functional volume to demonstrate its motion dexterity and positioning accuracy under the motion constraints. The functional volume is a cube of 150 mm×150 mm×150 mm, which is located at the center of the mockup peritoneal cavity. The mockup cavity can be seen in Figure 1 and Figure 10.

The experimental setup is shown in Figure 9(a) for measuring the movements of the trocar point and the gripper tip. A mockup trocar ring with an inner diameter of 10 mm was placed at the RCM point. The ring was suspended using elastic rubber bands to allow possible trocar motions. A marker was attached to the trocar ring and another marker was attached to the gripper to quantify their movements.

The functional volume and the positioning errors are shown in Figure 9(b), where the data are denoted in $\{W\} \equiv \{\hat{\mathbf{x}}_W, \hat{\mathbf{y}}_W, \hat{\mathbf{z}}_W\}$. The average tracking error is 4.21 mm, with the biggest error of 7.44 mm. During this process, the maximum movement of the RCM point, as shown in Figure 9(c), is 6.05 mm.

The motion errors could possibly be due to the misalignment between the SMARLT's stem and the $\hat{\mathbf{z}}_{D6}$-axis of the Denso manipulator, when the SMARLT is attached to the Denso's distal flange. Since the exchangeable effector is assembled into the actuation unit for quick switch of surgical end effector (where sliding fit was used), the angular misalignment can occur in any direction. A 1° misalignment

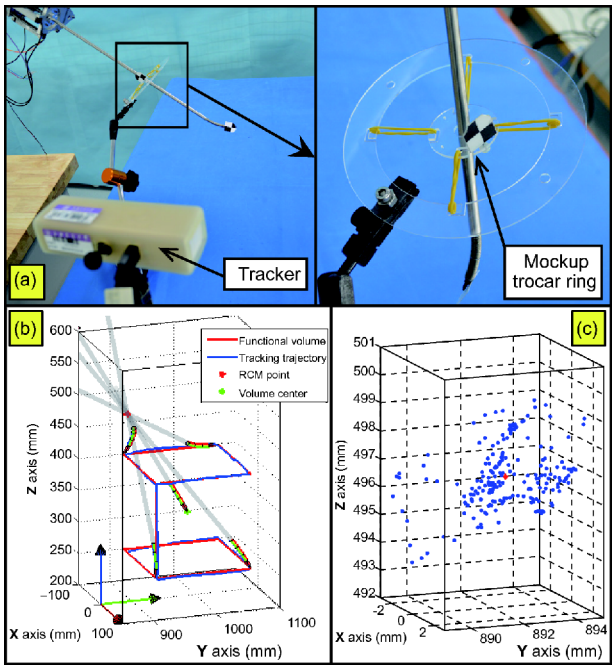

Figure 9 (Color online) Movement error quantifications. (a) The experimental setup; (b) positioning errors at the gripper tip while scanning the functional volume; (c) the tracked RCM positions.

corresponds to a position deviation of about 11.08 mm, due to the length of the stem. What's more, the friction between the stem and the mockup trocar ring dragged the trocar ring to increase the movement of the RCM point.

The position errors were not small. However, because the SMARLT-Denso system is fully teleoperated, the tracking errors become less critical with a human operator in the loop.

5.4 Task demonstrations

The SMARLT-Denso system was teleoperated to perform a few representative surgical tasks, including peeling, peg transferring, suture penetration, knot tying and weight lifting.

The Denso-SMARLT system was first teleoperated to peel a grape, as shown in Figure 10(a), to demonstrate the delicate motions of the SMARLT under motion constraints. The grape was fixed on a pole and its skin was sliced. The distal wrist was bent differently so that the gripper can poke into the grape and peel off the four skin parts.

The peg transfer task was performed as shown in Figure 10 (b). Four pegs with different heights were picked from the front and transferred to the back. The average transfer time for 10 trials of an inexperienced operator was about 120 s.

Tissue penetration using a half-inch circular suture was conducted, as shown in Figure 10(c). The gripper first gripped the tail of the suture and then positions the suture tip to the insertion point as well as adjusted the suture's orientation. During the penetration process, the gripper was teleoperated to rotate about the central axis of the suture so as

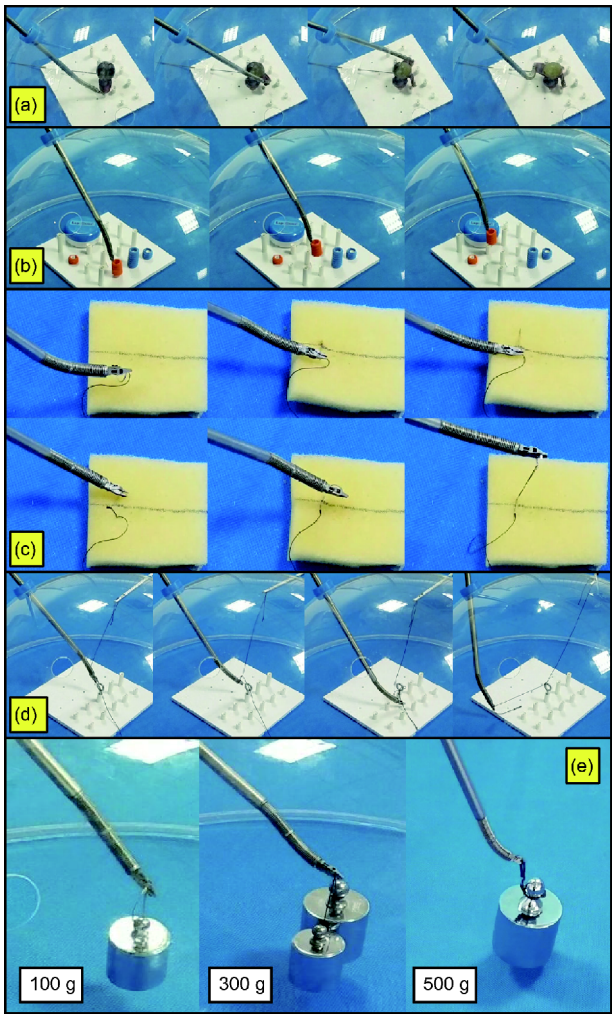

Figure 10 (Color online) Task demonstrations using the SMARLT-Denso system under motion constraints. (a) Grape peeling; (b) peg transferring; (c) tissue penetration on a mockup tissue; (d) knot tying; (e) weight lifting.

to minimize the penetration force and the tear to the mockup tissue. After the tip of the suture comes out from the other side of the mockup tissue, the gripper released the suture tail and gripped the tip. The suture was then pulled out from the tissue.

Knot tying was carried out as shown in Figure 10(d). An additional manual laparoscopic tool was used to assist this task by holding one end of the thread. A loop was first formed by moving the gripper around the thread. With the thread looped on the arm, the gripper gripped the thread on the other end. The gripper then pulled the thread through the thread loop to form a knot.

The payload capability of the SMARLT-Denso system was demonstrated through a few weight lifting experiments. Weights of 100, 300 and 500 g were successfully lifted, as shown in Figure 10(e). However, it can be seen that the continuum wrist's deformed shape was not circular anymore when the weight reached and exceeded 300 g.

6 Conclusions and future work

This study presents the development and experimental characterization of a modular robotic laparoscopic tool for MIS: the SMARLT.

A dual continuum mechanism concept is used to the design of the SMARLT to ensure reliability as well as achieve necessary distal dexterity, increased payload capability, and actuation modularity. While attached to a manipulator, the SMARLT-Denso system formed a continuum-rigid hybrid structure that makes full use of the advantages from each component: the continuum mechanism as a wrist for distal dexterity and other rigid parts for position accuracy and payload capability. The development of the SMARLT-Denso system widened the applicability of the dual continuum mechanism.

With the kinematics derived and the actuation compensation performed, the SMARLT-Denso system was teleoperated to perform typical laparoscopic tasks, such as tissue peeling, peg transferring, tissue penetration, and knot tying. Payload capabilities were demonstrated via a few weight lifting experiments. The movement accuracy of the SMARLT-Denso system was also experimentally quantified.

The obtained results suggest that the SMARLT can provide an alternative approach to realize robotic laparoscopic surgeries. The future efforts will mainly focus on: 1) the integration of a sterile barrier, 2) the incorporation of electrical surgical end effectors, and 3) improved packaging of the exchangeable effector and the actuation unit, in order to prompt possible commercialization opportunities.

This work was supported by the National Natural Science Foundation of China (Grant Nos. 51722507, 51435010 & 91648103), and the National Key R&D Program of China (Grant No. 2017YFC0110800).

Supporting Information

The supporting information is available online at tech.scichina.com and www.springerlink.com. The supporting materials are published as submitted, without typesetting or editing. The responsibility for scientific accuracy and content remains entirely with the authors.

1 Cuschieri A. Laparoscopic surgery: Current status, issues and future developments. Surgeon, 2005, 3: 125–138
2 Taylor R H. A perspective on medical robotics. Proc IEEE, 2006, 94: 1652–1664
3 Guthart G. Annual report 2014. 2015, 108
4 Navarra G, Pozza E, Occhionorelli S, et al. One-wound laparoscopic cholecystectomy. Br J Surg, 1997, 84: 695
5 Kalloo A N, Singh V K, Jagannath S B, et al. Flexible transgastric peritoneoscopy: A novel approach to diagnostic and therapeutic interventions in the peritoneal cavity. Gastrointestinal Endoscopy, 2004, 60: 114–117
6 Xu K, Zhao J, Fu M. Development of the sjtu unfoldable robotic system (surs) for single port laparoscopy. IEEE/ASME Trans Mechatron, 2015, 20: 2133–2145
7 Zhao J, Feng B, Zheng M H, et al. Surgical robots for spl and notes: A review. Minimally Invasive Ther Allied Technologies, 2015, 24: 8–17
8 Yamashita H, Kim D, Hata N, et al. Multi-slider linkage mechanism for endoscopic forceps manipulator. In: 2003 IEEE/RSJ International Conference on Intelligent Robots and Systems (IROS). IEEE, 2003. 2577–2582
9 Dombre E, Michelin M, Pierrot F, et al. Marge project: Design, modelling, and control of assistive devices for minimally invasive surgery. In: International Conference on Medical Image Computing and Computer-Assisted Intervention (MICCAI). DLR, 2004. 1–8
10 Van Meer F, Giraud A, Esteve D, et al. A disposable plastic compact wrist for smart minimally invasive surgical tools. In: IEEE/RSJ International Conference on Intelligent Robots and Systems (IROS). IEEE, 2005. 919–924
11 Ishii C, Kobayashi K. Development of a new bending mechanism and its application to robotic forceps manipulator. In: IEEE International Conference on Robotics and Automation (ICRA). IEEE, 2007. 238–243
12 Shin W H, Kwon D S. Surgical robot system for single-port surgery with novel joint mechanism. IEEE Trans Biomed Eng, 2013, 60: 937–944
13 Leonard S, Wu K L, Kim K L, et al. Smart tissue anastomosis robot (star): A vision-guided robotics system for laparoscopic suturing. IEEE Trans Biomed Eng, 2014, 61: 1305–1317
14 Hong M B, Jo Y H. Design of a novel 4-dof wrist-type surgical instrument with enhanced rigidity and dexterity. IEEE/ASME Trans Mechatron, 2014, 19: 500–511
15 Kanno T, Haraguchi D, Yamamoto M, et al. A forceps manipulator with flexible 4-dof mechanism for laparoscopic surgery. IEEE/ASME Trans Mechatron, 2015, 20: 1170–1178
16 Mitsuishi M, Sugita N, Pitakwatchara P. Force-feedback augmentation modes in the laparoscopic minimally invasive telesurgical system. IEEE/ASME Trans Mechatron, 2007, 12: 447–454
17 Xu K, Simaan N. An investigation of the intrinsic force sensing capabilities of continuum robots. IEEE Trans Robot, 2008, 24: 576–587
18 van den Bedem L, Hendrix R, Rosielle N, et al. Design of a minimally invasive surgical teleoperated master-slave system with haptic feedback. In: IEEE International Conference on Mechatronics and Automation (ICMA). IEEE, 2009. 60–65
19 Xu K, Simaan N. Intrinsic wrench estimation and its performance index for multisegment continuum robots. IEEE Trans Robot, 2010, 26: 555–561
20 Dalvand M, Shirinzadeh B, Shamdani A H, et al. An actuated force feedback-enabled laparoscopic instrument for robotic-assisted surgery. Int J Med Robotics Comput Assist Surg, 2014, 10: 11–21
21 Kim U, Lee D H, Yoon W J, et al. Force sensor integrated surgical forceps for minimally invasive robotic surgery. IEEE Trans Robot, 2015, 31: 1214–1224
22 Hagn U, Nickl M, Jörg S, et al. The dlr miro: A versatile lightweight robot for surgical applications. Industrial Robot, 2008, 35: 34–336
23 Berkelman P, Ma J. A compact modular teleoperated robotic system for laparoscopic surgery. Int J Robotics Res, 2009, 28: 1198–1215
24 Hannaford B, Rosen J, Friedman D W, et al. Raven-ii: An open platform for surgical robotics research. IEEE Trans Biomed Eng, 2013, 60: 954–959
25 Simaan N, Xu K, Kapoor A, et al. Design and integration of a telerobotic system for minimally invasive surgery of the throat. Int J Robot Res, 2009, 28: 1134–1153
26 Ding J, Goldman R E, Xu K, et al. Design and coordination kinematics of an insertable robotic effectors platform for single-port access surgery. IEEE/ASME Trans Mechatron, 2013, 18: 1612–1624
27 Simaan N, Bajo A, Reiter A, et al. Lessons learned using the insertable robotic effector platform (irep) for single port access surgery. J Robotic Surg, 2013, 7: 235–240
28 Taylor R H, Stoianovici D. Medical robotics in computer-integrated surgery. IEEE Trans Robot Automat, 2003, 19: 765–781
29 Kuo C H, Dai J S. Kinematics of a fully-decoupled remote center-of-motion parallel manipulator for minimally invasive surgery. J Med

Devices, 2012, 6: 021008
30 Hadavand M, Mirbagheri A, Behzadipour S, et al. A novel remote center of motion mechanism for the force-reflective master robot of haptic tele-surgery systems. Int J Med Robot Comp Assisted Surg, 2014, 10: 129–139
31 Azimian H, Patel R V, Naish M D. On constrained manipulation in robotics-assisted minimally invasive surgery. In: IEEE/RAS-EMBS International Conference on Biomedical Robotics and Biomechatronics (BIOROB). IEEE, 2010. 650–655
32 Lopez E, Kwok K W, Payne C J, et al. Implicit active constraints for robot-assisted arthroscopy. In: 2013 IEEE International Conference on Robotics and Automation (ICRA). IEEE, 2013. 5390–5395
33 Nasseri M A, Gschirr P, Eder M, et al. Virtual fixture control of a hybrid parallel-serial robot for assisting ophthalmic surgery: An experimental study. In: IEEE/RAS-EMBS International Conference on Biomedical Robotics and Biomechatronics (BIOROB). IEEE, 2014. 732–738
34 Xu K, Zhang H, Zhao J, et al. Design of a robotic laparoscopic tool with modular actuation. In: International Conference on Intelligent Robotics and Applications (ICIRA). 2017. 298–310
35 Okamura A M. Methods for haptic feedback in teleoperated robot-assisted surgery. Industrial Robot, 2004, 31: 499–508
36 Dubrowski A, Sidhu R, Park J, et al. Quantification of motion characteristics and forces applied to tissues during suturing. Am J Surgery, 2005, 190: 131–136
37 Berg D R, Kinney T P, Li P Y, et al. Determination of surgical robot tool force requirements through tissue manipulation and suture force measurement. In: Design of Medical Devices Conference. ASME, 2011. 1–4
38 Xu K, Fu M, Zhao J. An experimental kinestatic comparison between continuum manipulators with structural variations. In: IEEE International Conference on Robotics and Automation (ICRA). IEEE, 2014. 3258–3264
39 Zhao J, Zheng X, Zheng M, et al. An endoscopic continuum testbed for finalizing system characteristics of a surgical robot for notes procedures. In: IEEE/ASME International Conference on Advanced Intelligent Mechatronics (AIM). IEEE, 2013. 63–70
40 Xu K, Simaan N. Analytic formulation for the kinematics, statics and shape restoration of multibackbone continuum robots via elliptic integrals. J Mech Robot, 2010, 2: 1–13
41 Webster R J, Jones B A. Design and kinematic modeling of constant curvature continuum robots: A review. Int J Robotics Res, 2010, 29: 1661–1683
42 Siciliano B, Khatib O. Handbook of Robotics. Springer, 2008
43 Bettini A, Marayong P, Lang S, et al. Vision-assisted control for manipulation using virtual fixtures. IEEE Trans Robot, 2004, 20: 953–966
44 Nenchev D N. Restricted jacobian matrices of redundant manipulators in constrained motion tasks. Int J Robotics Res, 1992, 11: 584–597
45 Xu K, Simaan N. Actuation compensation for flexible surgical snake-like robots with redundant remote actuation. In: IEEE International Conference on Robotics and Automation (ICRA). IEEE, 2006. 4148–4154